Residual Overturning Circulation and Associated Water-Mass Transformation in the East/Japan Sea

YUJIN KIM,[a] HAJOON SONG,[a,b] KYUNGHUN HAN,[c] SOON-IL AN,[a,b] YOUNG-GYU PARK,[d] AND JOHN MARSHALL[e]

[a] *Department of Atmospheric Sciences, Yonsei University, Seoul, South Korea*
[b] *Division of Environmental Science and Engineering, Pohang University of Science and Technology, Pohang, South Korea*
[c] *3rd Fleet Command, ROK Navy, Gyeryong, South Korea*
[d] *Ocean Circulation and Climate Research Department, Korea Institute of Ocean Science and Technology, Busan, South Korea*
[e] *Department of Earth, Atmospheric and Planetary Sciences, Massachusetts Institute of Technology, Cambridge, Massachusetts*

(Manuscript received 8 July 2024, in final form 18 November 2024, accepted 5 February 2025)

ABSTRACT: The East/Japan Sea (EJS), a marginal sea in the northwest Pacific, has marked isopycnal slopes, especially during winter, implying a store of potential energy available for baroclinic instability and hence, perhaps, a significant role for eddy processes in shaping the residual (mean plus eddy) overturning circulation. Here, for the first time, we compute the residual overturning circulation in the EJS in a high-resolution simulation and relate it to water-mass transformation processes due to air–sea fluxes and interior mixing. A sizable eddy-driven circulation is indeed found in the vicinity of tilted isopycnals. Wintertime surface buoyancy loss facilitates a volume flux toward higher-density classes, with latent heat loss being the main contributor and sensible heat loss also playing a role. The densification of northward subsurface flow is associated with diapycnal mixing. The water-mass formation rate, derived from the transformation rate, identifies upwelling and downwelling to the south and north of the subpolar front near 39.5°N, respectively, consistent with the broad pattern of residual overturning circulation.

SIGNIFICANCE STATEMENT: In the East/Japan Sea (EJS), we computed the residual overturning circulation for the first time and linked it to water-mass transformation through the air–sea fluxes and interior mixing. We found a significant eddy-driven circulation with tilted isopycnals, especially during winter. The residual overturning circulation orchestrates with the surface buoyancy flux. In particular, the wintertime buoyancy loss, mainly driven by latent heat, relates the volume flux to higher-density classes. Furthermore, we identify upwelling and downwelling patterns around the subpolar front based on the water-mass formation rate, which is consistent with the overall residual overturning circulation. These findings are crucial for understanding the role of eddies and air–sea buoyancy fluxes in the EJS circulation and provide a guide to the projected changes in the ocean circulation under a warming climate.

KEYWORDS: Atmosphere-ocean interaction; Diapycnal mixing; Eddies; Meridional overturning circulation; Heat budgets/fluxes; Regional models

1. Introduction

The East/Japan Sea (EJS), a semienclosed marginal sea in the northwest Pacific bordered by South Korea, Japan, and Russia, is the site of a wide range of oceanic processes. Flowing in from the south, a warm water mass enters the EJS at a rate of roughly 2–3 Sv (1 Sv $\equiv 10^6$ m^3 s^{-1}) through the shallow Korea Strait (<250 m deep) (Isobe 2008). For most of the year, except during a few summer months, this water mass loses buoyancy in the EJS before exiting into the northwest Pacific through two narrow straits, the Soya Strait (<150 m deep) and the Tsugaru Strait (<200 m deep). The EJS features a subpolar front (SPF), hosting a cyclonic gyre to its north and an anticyclonic gyre to its south, with intensified currents on the western margins (Fig. 1a). Sea ice forms seasonally in the proximity of the northern coast, resulting in the development of a dense water mass and ventilation, as evidenced by a notable presence of dissolved oxygen in the deep ocean (Kim et al. 2001; Talley et al. 2006; Yoon et al. 2018, Fig. 1a). These diverse features collectively position the EJS as a miniature representation of the global ocean (Ichiye 1984; Kim et al. 2001, 2002; Talley et al. 2003; Riser and Jacobs 2005; Min and Warner 2005).

The distinct overturning circulation of the EJS sets it apart from other marginal seas (Gamo 1999; Kim et al. 2001). At the surface, the Tsushima Warm Current (TWC) and East Korea Warm Current (EKWC) transport warm, saline waters northward, while the North Korea Cold Current (NKCC) and Liman Cold Current (LCC) transport cold, low-salinity waters southward (Fig. 1b). Subsurface observations from profiling floats and moored current meters reveal the existence of two cyclonic gyres, one in the Japan Basin (JB) and the other in the Ulleung/Tsushima Basin (UTB), at 800 dbar and below (Danchenkov and Riser 2000; Senjyu et al. 2005; Choi and Yoon 2010; Park and Kim 2013). The subsurface circulation is constrained by potential vorticity conservation, particularly in the steep slope region of the JB. This constraint is less clear in

Supplemental information related to this paper is available at the Journals Online website: https://doi.org/10.1175/JPO-D-24-0100.s1.

Corresponding author: Hajoon Song, hajsong@yonsei.ac.kr

DOI: 10.1175/JPO-D-24-0100.1

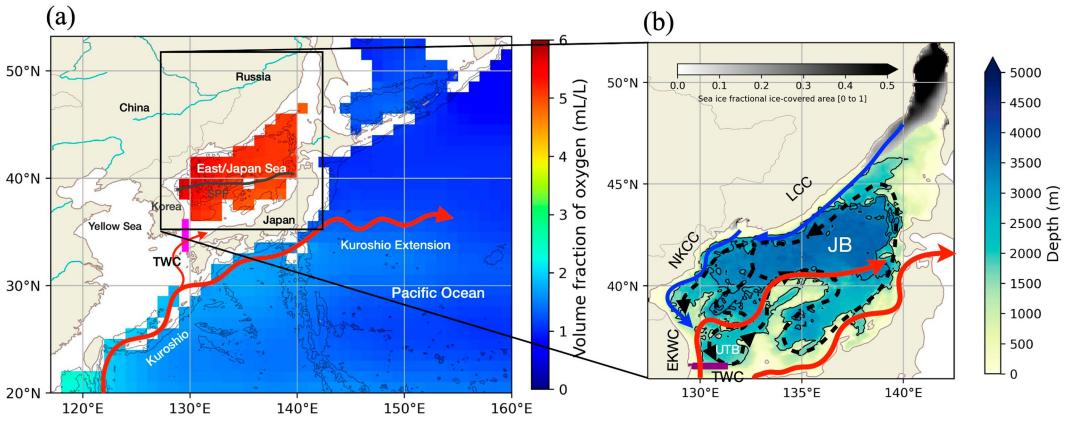

FIG. 1. (a) Model domain, the volume fraction of oxygen (mL L^{-1}) at 1000-m depth (*WOA2013* V2, Levitus et al. 2015) and (b) bathymetry and currents of the EJS. The magenta line in (a) is the section across which the volume transport of the Korea Strait calculated in Fig. S4. The purple line in (b) marks the position of the observed section taken by the National Institute of Fisheries Science (NIFS). The dark shading in (b) represents the modeled ice-covered region during the 1996–2015 average winter (December–February), where the fractional ice-covered area [0–1] exceeds 0. Contours represent the 1500- and 3000-m isobaths.

the UTB, where the circulation is weaker and active mesoscale eddies are present (Choi and Yoon 2010). The time–space averaged deep mean current is $O(1)$ cm s^{-1} with elevated speeds near the peripheries of the basins where steep slopes exist (Senjyu et al. 2005; Choi and Yoon 2010; Park and Kim 2013).

Various numerical modeling studies have been conducted in the EJS. The Princeton Ocean Model (POM) result was compared with observational data, and the significant influence of large-scale wind patterns on the depth of the mixed layer, intermediate water formation, and deep convection was explored (Mooers et al. 2006). The Geophysical Fluid Dynamics Laboratory Modular Ocean Model (GFDL MOM) has been utilized to calculate water-mass formation rates and turnover times of water masses (Kawamura et al. 2007). A nonhydrostatic numerical model has also been applied to investigate the influence of wind stress and surface cooling on the subpolar front (Fig. 1a) in the EJS (Yoshikawa et al. 2012). Spatiotemporal variations of sea surface temperature (SST), currents, and the subpolar front in the EJS over an extended period (130 000 years) were examined using the Research Institute for Applied Mechanics Ocean Model (RIAMOM) at a horizontal resolution of 1/6° with 50 vertical layers (Choi et al. 2012). RIAMOM with the same horizontal resolution but 102 vertical layers showed that geothermal heating in the EJS enhances both deep and surface circulations, as well as overturning (Park et al. 2013). A study using the Regional Ocean Modeling System (ROMS) with a horizontal resolution of approximately 3 km and 41 vertical layers identified intrinsic variability as the dominant factor contributing to interannual variability in surface circulation in the EJS (Choi et al. 2018).

Overturning circulation connects surface and subsurface oceans and plays a significant role in the transport of oxygen, carbon, heat, nutrients, freshwater, and salinity (Plumb and Mahlman 1987). One prominent example is the Atlantic meridional overturning circulation (AMOC), which plays a major role in the global transport of heat, carbon, and freshwater (Buckley and Marshall 2016). Research on overturning circulation is ongoing in various regions of the global ocean, including the Southern Ocean, Mediterranean Sea, Indian Ocean, South China Sea, the Gulf of Arabia, Yellow Sea, and the EJS (Wilson et al. 2022; Al-Shehhi et al. 2021; Pinardi et al. 2019; Jayasankar et al. 2019; Wang et al. 2016; Yao et al. 2014). In particular, Han et al. (2020) analyzed Hybrid Coordinate Ocean Model (HYCOM) reanalysis data to investigate the meridional overturning circulation in the EJS from 1993 to 2012, revealing a decadal pattern of overturning circulation. Han et al. (2021) calculated the associated overturning time scale. However, these studies focused on the Eulerian-mean overturning circulation leaving the role of the eddy-driven circulation unexplored.

The residual circulation encompasses not only the mean circulation but also the circulation driven by eddies (Andrews et al. 1987; Marshall and Radko 2003). The concept of the residual circulation has been employed to investigate the circulation in various regions such as the Southern Ocean, Atlantic and Indo-Pacific Oceans, the Weddell Sea, the Gulf of Arabia, and the Mediterranean Sea (Marshall and Radko 2003; Cessi 2019; Stewart 2021; Al-Shehhi et al. 2021; Pinardi et al. 2019). The magnitude of the eddy-driven circulation can be comparable to that of the mean circulation but with the opposite sign, leading to a significant cancellation of the Eulerian overturning circulation (Abernathey et al. 2011), hence the name residual. The EJS has steep isopycnals near the surface in winter, suggesting considerable baroclinic instability and the prospect of a large eddy-driven circulation. Hence, studying the residual circulation in the EJS provides a deeper understanding of tracer transports in the EJS (Kim et al. 2001; Talley et al. 2006; Yoon et al. 2018).

The overturning circulation can be quantified by diagnosing the water-mass formation rate, where air–sea buoyancy fluxes

drive water-mass transformation, potentially resulting in the convergence or divergence of volume flux. In this case, employing the framework outlined in Walin (1982) offers valuable insights into how ocean circulation evolves via water-mass transformation, as evidenced in previous studies (Marshall et al. 1999; Koch-Larrouy et al. 2008; Nishikawa et al. 2013; Abernathey et al. 2016; Xu et al. 2018; Groeskamp et al. 2019; Al-Shehhi et al. 2021). Kang and Mooers (2005) examined the annual mean water-mass transformation in the EJS using POM and related the diapycnal volume flux toward higher-density classes to the buoyancy loss at the surface. However, the seasonality of the water-mass transformation rate and a detailed breakdown of the transformation into surface fluxes have not yet been explored. Analyzing water-mass transformation on a component basis is expected to provide us with a more detailed understanding of how water masses change through the interaction between the atmosphere and ocean at the sea surface.

In this study, we analyze the residual circulation and water-mass transformation rates in the EJS in a high-resolution ocean model. Section 2 contains the details on the model and briefly introduces the residual circulation and water-mass transformation analysis. Simulated residual circulation, water-mass transformation, and formation in the EJS are then presented in section 3. Section 4 summarizes our findings and concludes.

2. Numerical simulation of EJS and analysis methods

a. Configuration of numerical ocean model

We conducted simulations of the EJS using the Massachusetts Institute of Technology General Circulation Model (MITgcm) (Marshall et al. 1997a,b), a z^*-coordinate model based on the Arakawa C grid (Arakawa and Lamb 1977) that numerically solves the primitive equations under the Boussinesq approximation. Utilizing a global LLC_1080 configuration as the basis, the model was configured over the northwest Pacific, spanning from 20° to 53.2°N in the meridional direction and from 117° to 159.6°E in the zonal direction. This area includes marginal seas such as the EJS, the Yellow Sea, and the South Sea, as well as the East China Sea, the Bohai Sea, and the northern Philippine Sea (Fig. 1). The horizontal grid resolution is approximately 1/12° (about 0.08°), and the longitudinal grid spacing decreases northward to about 0.05°. There are 90 vertical layers with a minimum spacing of 1 m near the surface and 52 layers within the top 1000 m.

The bathymetric data were extracted from the General Bathymetric Chart of the Oceans 2014 grid (Weatherall et al. 2015). The initial temperature and salinity fields were created using *World Ocean Atlas 2013*, version 2 (*WOA2013* V2), while other initial fields and lateral boundary conditions were created using the Ocean Reanalysis System 5 (ORAS5) dataset, at a spatial and temporal resolution of a 0.25° and monthly averages, respectively (Locarnini et al. 2013; Zweng et al. 2013; Zuo et al. 2019). Tidal forcing was introduced at the lateral boundaries as additional normal flows from 10 tidal constituents (M2, S2, N2, K2, K1, O1, P1, Q1, Mf, and Mm), derived from the Oregon State University (OSU) Tidal Prediction Software (OTPS) data (Egbert and Erofeeva 2002). Momentum, heat, and freshwater fluxes at the sea surface are calculated using bulk formulae (Large and Pond 1981, 1982) with the near-surface atmospheric fields taken from the fifth major global reanalysis produced by ECMWF (ERA5) dataset, featuring 0.25° spatial resolution and hourly data (Hersbach et al. 2023, 2020). The resolution of the ERA5 data could present a potential limitation, as it shows greater eddy kinetic energy compared to observations (Fig. S5 in the online supplemental material).

Daily river runoff data are derived from the Japanese 55-year Reanalysis for driving ocean–sea ice models (JRA55-do), known for generally high Willmott skill scores (Feng et al. 2021; Tsujino et al. 2018). If grid cells with nonzero runoff are masked during the interpolation from the native to the model grid, the corresponding runoff amounts are redistributed to neighboring wet points. Additionally, sea surface salinity is relaxed to the monthly climatological values obtained from *WOA2013* V2 with a relaxation time scale of 1 month (Zweng et al. 2013).

The simulation proceeds from 1 January 1996 to 31 December 2015. During the integration, the vertical mixing is computed using the nonlocal *K*-profile parameterization (KPP) scheme (Large et al. 1994). The growth and melt of sea ice in the northern part of the domain are represented using a sea ice model (Losch et al. 2010) after being initialized with ORAS5 data. The simulation has been extensively evaluated through comparison with observations and has been shown to successfully capture many features including sea surface height anomalies, SST, the vertical structure of temperature and salinity, eddy kinetic energy, and the volume transport across the Korea Strait (see the supplemental information). Additionally, the LAYERS diagnostic package is implemented with 200 layers spanning the potential density range from 10 to 30 kg m^{-3}. LAYERS computes the volume transport along isopycnals and associated thermodynamic processes at each model time step. This permits a direct calculation of overturning circulation and water-mass transformation rate. To ensure the robustness of the simulation, alternative model configurations and input data were also tested, but the results are not systematically different (see Table A1, Fig. A1 in the appendix).

b. Calculation of residual overturning circulation

We compute the residual overturning streamfunction to quantify the overturning circulation associated with enhanced mesoscale eddy activity in the region of tilted density surfaces in the EJS. The mass transport in a chosen density class can be written as

$$\overline{vh} = \overline{v}\,\overline{h} + \overline{v'h'}, \tag{1}$$

where v is the meridional velocity, h is the thickness of the density layer, and overbar and prime are the time mean and deviation, respectively, such that $v = \overline{v} + v'$ and $h = \overline{h} + h'$ (Zika et al. 2009; Marshall and Speer 2012; Pinardi et al. 2019). The mass transport in Eq. (1) can be represented using a streamfunction:

$$\psi_{\text{res}} = \overline{\psi} + \psi^*. \tag{2}$$

For the streamfunction to be defined, the flow must be nondivergent, meaning there should be no zonal inflow or outflow, and it must be steady. Thus, at the latitude and depth of the Tsugaru Strait, the streamfunction cannot be defined. At a given latitude y and density $\tilde{\sigma}$, ψ_{res}, the meridional residual overturning streamfunction averaged over time t_0 and t_1, can be computed as

$$\psi_{\text{res}}(y, \tilde{\sigma}) = -\overline{\int_{x_{\min}}^{x_{\max}} \int_{-H}^{z(x,y,\tilde{\sigma},t)} v(x, y, z', t) dz' dx}, \tag{3}$$

where $x_{\min}$ and $x_{\max}$ denote the longitudinal range of the EJS region and $-H$ represents the bottom depth. The LAYERS package in MITgcm carries out this calculation with precision because vh is computed in every density class at every model time step. The Eulerian streamfunction $\overline{\psi}$, which represents the mean overturning circulation, is calculated as

$$\overline{\psi}(y, z) = -\int_{x_{\min}}^{x_{\max}} \int_{-H}^{z} \overline{v(x, y, z', t)} dz' dx, \tag{4}$$

following a similar approach to that of Zika et al. (2012). The eddy-induced streamfunction ψ^* is computed as the difference between ψ_{res} and $\overline{\psi}$.

Alternatively, ψ_{res} can also be written as the sum of the contributions from the zonally averaged mean Eulerian flow $\langle\overline{\psi}\rangle$, standing eddies ψ_{SE}, and transient eddies ψ_{TE} (Dufour et al. 2012) as follows:

$$\psi_{\text{res}}(y, \sigma) = \langle\overline{\psi}\rangle(y, \sigma) + \psi_{\text{SE}}(y, \sigma) + \psi_{\text{TE}}(y, \sigma), \tag{5}$$

where

$$\langle\overline{\psi}\rangle + \psi_{\text{SE}} = \int_{x_{\min}}^{x_{\max}} \int_{-H}^{\overline{z}(x,y,\sigma)} \overline{v}(x, y, \sigma) dz' dx, \tag{6}$$

$$\langle\overline{\psi}\rangle = \int_{x_{\min}}^{x_{\max}} \int_{-H}^{\langle\overline{z}\rangle(y,\sigma)} \langle\overline{v}\rangle(y, \sigma) dz' dx. \tag{7}$$

The angle brackets denote a zonal average at constant depth.

c. Water-mass transformation

Flow entering from the south crosses isopycnals toward higher density within the EJS. This diapycnal volume flux requires density changes by either surface forcing and/or diapycnal mixing. We can quantify these processes using the framework initially proposed by Walin (1982) and developed in subsequent literature (e.g., Marshall et al. 1999; Nishikawa et al. 2013; Abernathey et al. 2016; Groeskamp et al. 2019).

The diapycnal volume flux integrated over the isopycnal area $\mathscr{A}_\sigma$ can be computed as

$$A(\sigma, t) = \iint_{\mathscr{A}_\sigma(\sigma,t)} (\mathbf{v} - \mathbf{v}_\sigma) \cdot \hat{\mathbf{n}}_\sigma d\mathscr{A}, \tag{8}$$

where $\mathbf{v}$ and $\mathbf{v}_\sigma$ are the velocities of the fluid and the isopycnal σ, respectively, and $\hat{\mathbf{n}}_\sigma$ is the unit vector normal to the isopycnal surface. The diapycnal volume flux $A(\sigma, t)$, or the net transformation rate, can be decomposed into components associated with air–sea flux and diffusive fluxes across isopycnals as follows:

$$A = F - \frac{\partial D}{\partial \sigma}, \tag{9}$$

$$= \frac{\partial B_s}{\partial \sigma} - \frac{\partial D}{\partial \sigma}. \tag{10}$$

Here, B_s is the surface density flux and D is the diffusive density flux across an isopycnal surface. The first term in Eq. (10) is identified as the water-mass transformation rate and can be expressed in terms of the surface buoyancy flux as follows:

$$B_s(\sigma, t) = -\frac{\rho_0}{g} \iint_{\mathscr{A}_s(\sigma,t)} \mathscr{B}_s d\mathscr{A}, \tag{11}$$

where $\mathscr{A}_s$ is the surface area of the ocean with a density of σ, ρ_0 is the reference density, g is the gravity, and $\mathscr{B}_s$ is the surface buoyancy flux defined as

$$\mathscr{B}_s = \frac{g}{\rho_0}\left[\frac{\alpha}{c_w}(\mathscr{Q}_{\text{SW}} + \mathscr{Q}_{\text{LW}} + \mathscr{Q}_L + \mathscr{Q}_S) + \rho_0 \beta S \mathscr{F}_{\text{FW}}\right]. \tag{12}$$

In Eq. (12), $\mathscr{Q}_{\text{SW}}$, $\mathscr{Q}_{\text{LW}}$, $\mathscr{Q}_L$, and $\mathscr{Q}_S$ represent heat fluxes (upward being positive) from shortwave radiation, longwave radiation, latent heat, and sensible heat, respectively. The α is the thermal expansion coefficient, c_w is the heat capacity of water, S is the surface salinity, and $\mathscr{F}_{\text{FW}}$ is the net freshwater flux that includes evaporation, precipitation, river runoff, and sea ice–related processes. Although sea ice is present in the EJS, its area is small and is expected to have a negligible contribution to water-mass transformation; therefore, it was not analyzed separately. The unit of buoyancy flux $\mathscr{B}_s$ is (m s^{-2}) × (m s^{-1}), that of the area-integrated surface density flux B_s is (kg m^{-3}) × (m^3 s^{-1}), and the units of A and F are m^3 s^{-1}.

3. Results

a. The residual overturning circulation

The density vertical structure is first evaluated since the meridional residual overturning streamfunction is computed in density space. Seasonal variability is indeed evident, particularly at densities lower than 27 kg m^{-3}. In summer, the isopycnals in the top 50 m are generally flat and tightly spaced in the vertical, indicating strong stratification (Fig. 2a). In contrast, the winter isopycnals have steeper slopes in the top 100 m and are relatively widely spaced (Fig. 2b). Moreover, isopycnals outcrop between approximately 36°–42°N, suggesting that perhaps the top 100 m of the ocean is directly influenced by air–sea interaction in winter. Below 100 m, the isopycnals have little seasonal variability. These distinct differences in the upper-ocean density potentially result in different meridional overturning circulations in the EJS.

The annually averaged residual overturning streamfunctions are calculated using vh in density space and are plotted in Fig. 3a. Positive (negative) values indicate clockwise (counterclockwise) circulation around the contours. Unlike in

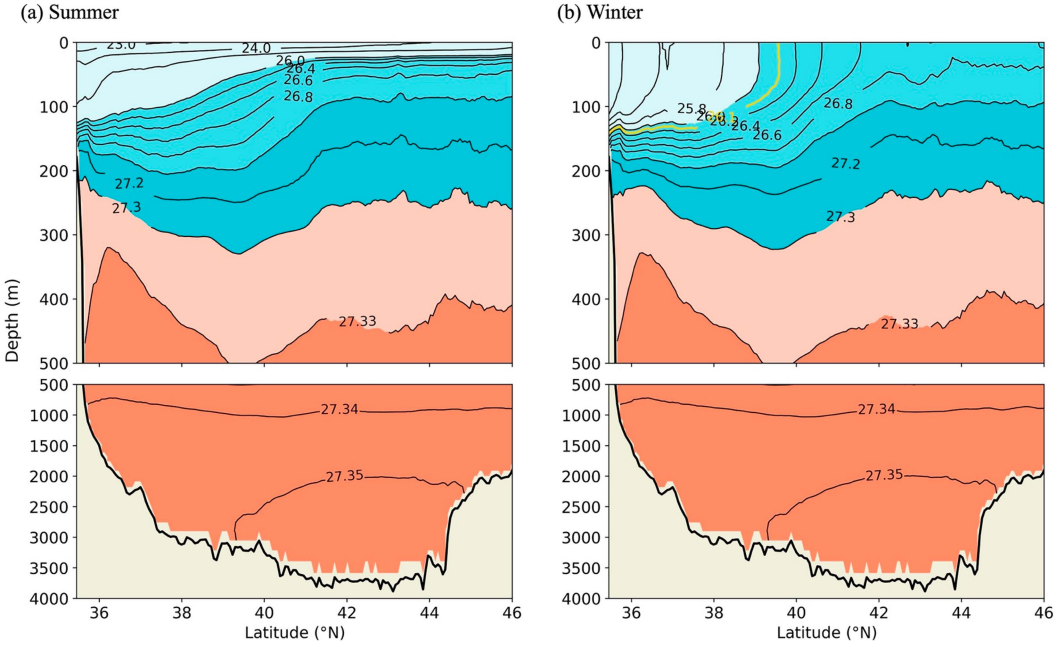

FIG. 2. Zonally averaged density (kg m^{-3}) in the EJS during (a) summer (June–August) and (b) winter (December–February). To better visualize the density structure, some contours have been drawn at irregular intervals but are labeled. The top 500 m is magnified for clarity.

a closed basin, the EJS does not have a streamfunction approaching zero at the surface. Instead, large negative values signify inflows from the south and outflows at the Tsugaru and Soya Straits near 41.5° and 46°N, respectively. In these straits, the flow is divergent, and so the area is masked. As water masses in the upper ocean move northward, density increases and layers become shallower. For example, the 25.5 kg m^{-3} water mass near the southern edge is found deeper than 100 m, but its density and depth near the Tsugaru Strait—at 41.5°N—are ~26.3 kg m^{-3} and shallower than 100 m, respectively (green contours in Fig. 3c). This density increase stems from diapycnal mixing, as described below.

Beneath the northward flow lies the clockwise overturning cell, indicated by a positive residual overturning streamfunction. This cell spans a broad range of density near the southern edge and contracts northward. The upper branch of the cell with density lower than 26.7 kg m^{-3} experiences density increases, while the lower part tends to maintain its density (Fig. 3a). The water mass within the density range of 26.5–27 kg m^{-3} moves northward (40°–44°N) and transitions to a higher-density class, which feeds the southward flow at a higher-density range. However, the deep/bottom water formation, which can be inferred from the high oxygen concentration at 1000-m depth in the EJS as shown in Fig. 1a, is not evident in this residual overturning streamfunction. This suggests that the deep/bottom water formation might not be well presented in the model.

The streamfunction for the eddy-driven circulation is computed by subtracting the Eulerian streamfunction $\overline{\psi}$ from the residual overturning streamfunction ψ_{res}. The residual overturning streamfunction, calculated in density space, is first projected onto depth using the zonally averaged density field for this purpose. This projection is performed using the monthly averaged fields, and the eddy-driven streamfunction is obtained by averaging from a 20-yr simulation (Fig. 3c).

The sense of the eddy-driven circulation is to slump the isopycnals (green contours in Fig. 3c)—that is, to return them to the horizontal. The positive ψ^* (clockwise circulation) corresponds to isopycnals sloping upward to the north, while a negative ψ^* (counterclockwise circulation) is observed where isopycnals slope downward moving north. Over latitudes 36°–40°N, the eddy-driven circulation acts to flatten the sloping density lines (Fig. 3c). This ψ^* is about half the size of $\overline{\psi}$ but of opposite sign, suggesting that eddy-driven circulation compensates for the mean circulation (Figs. 3b,c). In other words, ignoring eddy-driven circulation would lead to a significant overestimation of the northward volume transport, especially to the south of 41.5°N. Especially in winter, the isopycnals are almost vertical (Fig. 2b), suggesting that the eddy-driven circulation could be expected to intensify to counteract this steepness. The isopycnals are generally flat to the north of 41.5°N where the eddy-driven streamfunction diminishes. This abrupt change in isopycnal slope is associated with the subpolar front. To the south of this front, relatively warm water flows into the EJS and experiences buoyancy loss to the atmosphere before exiting through the Tsugaru Strait. In contrast, relatively well-mixed water is exposed to the atmosphere to the north of the front, with small isopycnal slopes and eddy-driven overturning. The subsurface (below 400 m) eddy-driven streamfunction is much smaller compared to the values above 300 m, and neither the isopycnals nor the eddy-driven streamfunction shows large seasonal variation (not shown).

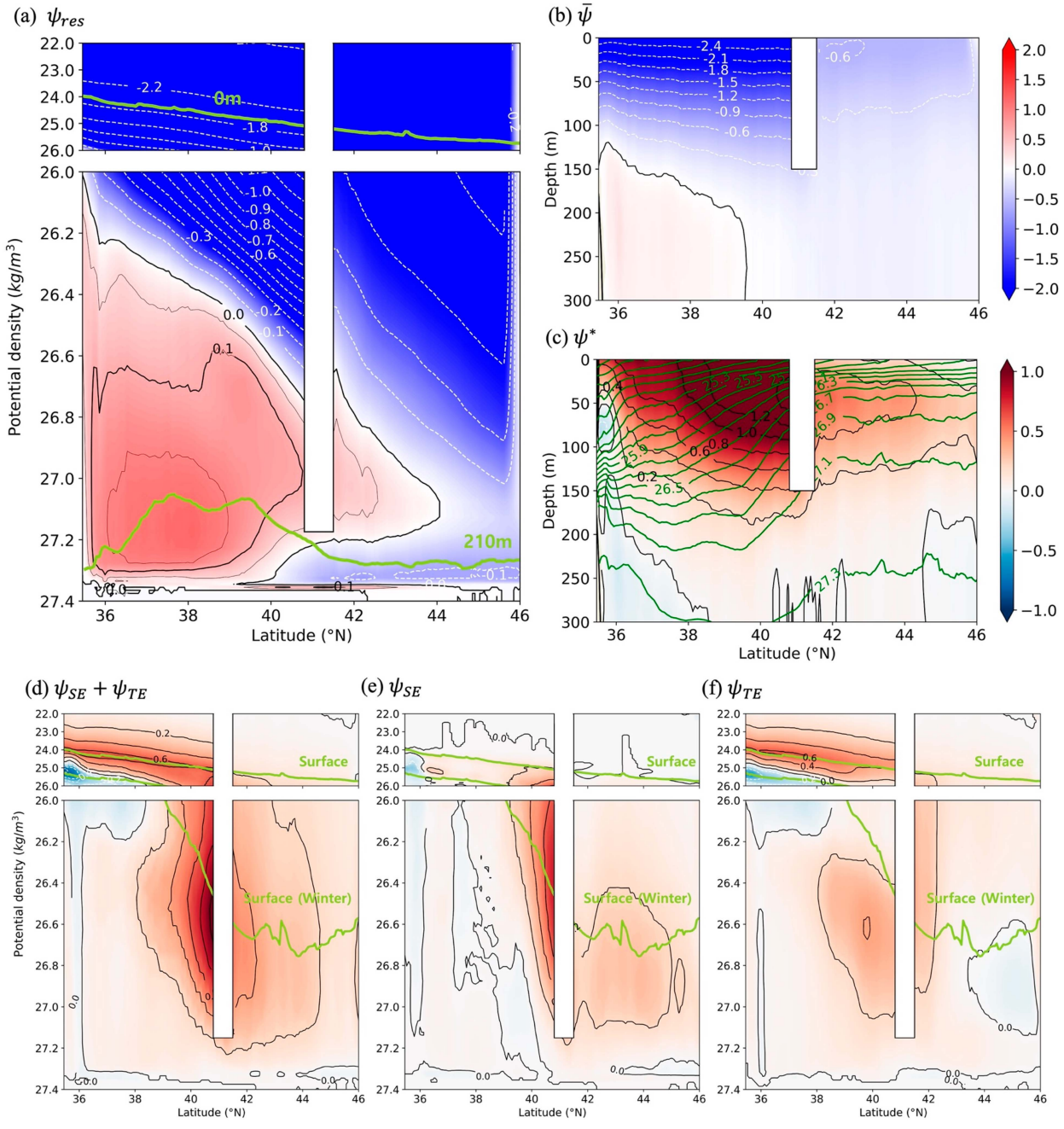

FIG. 3. (a) Meridional residual overturning streamfunction (Sv) averaged over the period 1996–2015. Thick and thin black contours are at 0.1- and 0.05-Sv intervals, respectively. (b) The Eulerian streamfunction $\overline{\psi}$ (Sv) and (c) eddy-driven circulation ψ^* calculated as $\psi^* = \psi_{\text{res}} - \overline{\psi}$. Dark green lines are the mean density contours (kg m^{-3}). (d) Streamfunction (Sv) associated with both standing and transient eddies ($\psi_{\text{SE}} + \psi_{\text{TE}}$), (e) standing eddies ψ_{SE}, and (f) transient eddies ψ_{TE} in density coordinates. The light green lines in (a) represent the mean density at the surface and at 210 m. The light green lines in (d)–(f) represent the mean density at the surface averaged over the entire year and in winter (December–February).

The eddy-driven circulation in density coordinates generally aligns with the patterns observed in the eddy-driven circulation described above (Figs. 3c,d). Both figures reveal a relatively strong eddy-driven circulation south of the Tsugaru Strait and a weaker circulation to its north. While standing eddies make a prominent contribution near the strait, transient eddies have a greater impact in the region south of 40°N (Figs. 3e,f). This corresponds to the tilted isopycnals near the surface in winter, suggesting that the intensified eddy-driven circulation acts to flatten the winter isopycnals (Fig. 3f). North

of the Tsugaru Strait, standing eddies are the primary contributors, with transient eddy effects largely confined to areas closer to the strait.

b. Water-mass transformation

The residual overturning circulation is associated with density changes which are now analyzed using the water-mass transformation framework presented in section 2c. The water-mass transformation rate [F in Eq. (9)] facilitates a diapycnal volume flux [A in Eq. (8)], which can be computed from $\mathbf{v}$ and $\mathbf{v}_\sigma$. The seasonally averaged water-mass transformation rates have opposite signs, negative in summer and positive in winter (see Figs. 4c,d).

The summertime water-mass transformation rates range between −150 and −50 mSv (1 mSv = 10^3 m^3 s^{-1}), with little spatial variation compared with that of wintertime (from 0 to 250 mSv) (Figs. 4c,d). Since the surface flow progresses toward higher density (positive $\mathbf{v}$) in summer (with inflow through the Korea Strait, as shown in Fig. S4), negative F implies a northward $\mathbf{v}_\sigma$ which is larger than $\mathbf{v}$. The negative F in summer stems from buoyancy gain due to surface heat flux (Figs. 4c,e,g). In contrast, the F in winter is positive (Fig. 4d). This supports a positive area-integrated $(\mathbf{v} - \mathbf{v}_\sigma)\cdot \hat{\mathbf{n}}_\sigma$, comprising a positive $\mathbf{v}$ and a negative $\mathbf{v}_\sigma$ due to northward flow and surface buoyancy loss, respectively. This positive water-mass transformation rate due to strong wintertime surface buoyancy loss allows the northward flow toward higher-density classes (Fig. 4b).

The contribution from heat loss dominates that due to freshwater flux in winter (Figs. 4d,f,h). The maximum rate is found near the southeastern part of the EJS, while it approaches zero in the northern part of the EJS, resulting in the most significant gradient near 40°N (Fig. 4d). This heterogeneous spatial distribution of F can be linked to SST (Figs. S2c,d). The warm water mass entering the EJS through the Korea Strait flows mainly along the west coast of Japan, accompanied by elevated buoyancy loss. This process accounts for the greater positive water-mass transformation rate in the southeastern part of the EJS.

The water-mass transformation rate is further analyzed by partitioning it into surface heat and freshwater flux contributions (Fig. 5). In summer, transformation occurs in the density range from roughly 20 to 26 kg m^{-3}. The dominant contributor is shortwave radiation which decreases surface density (Fig. 5a). Additionally, precipitation contributes to negative rates. In contrast, longwave radiation, latent heat flux, and evaporation result in discernible positive transformation rates (Fig. 5a). The contribution from sensible heat flux is insignificant, suggesting that surface air temperature and SST are similar in summer.

In winter, the total water-mass transformation rates are positive in density ranges from approximately 24.5 to 27.4 kg m^{-3} (Fig. 5b). This is a somewhat narrower range than in summer, but the transformation rates are of higher magnitude. As in summer, shortwave radiation and precipitation result in negative rates. However, the contribution from shortwave radiation is approximately half that in summer. On the other hand, the rate from latent heat flux shows a nearly fourfold increase, surpassing the combined contributions of both shortwave radiation and precipitation (Fig. 5b). This elevated contribution from latent heat flux is a consequence of dry, strong northwesterly winds blowing over the warm water from the south. Interestingly, the sensible heat flux contribution exceeds that of solar radiation (Fig. 5b). These notably high rates are due to air temperature which drops markedly below SST in winter. The wind is also an important contributor to this increase: The average wind speed in winter was 1.64 times greater than in summer in the EJS. Surprisingly, longwave radiation and evaporation also induce positive water-mass transformation rates. In particular, the contribution of longwave radiation is even greater than that of shortwave radiation.

The diapycnal volume flux due to diffusive density flux, $-\partial D/\partial\sigma$ in Eq. (9), at the base of the mixed layer is positive, and in both summer and winter is an order of magnitude smaller than that due to surface density fluxes (Fig. 5c). This is crucial to understanding the residual overturning circulation. Northward flow experiences densification below the surface (Fig. 3a) due to the diffusive flux. In both seasons, the diffusive flux of potential temperature explains most of $-\partial D/\partial\sigma$, contributing nearly 90% in winter (solid purple line in Fig. 5c). The consistently positive $-\partial D/\partial\sigma$ contrasts with the seasonally varying sign in the water-mass transformation rate (Figs. 5a,b). The diffusive density flux mitigates negative transformation in summer and reinforces positive wintertime water-mass transformation, accelerating mixed-layer density increase in the winter.

c. Water-mass formation and upwelling/downwelling in winter

The variation in water-mass transformation rate across density space reflects the convergence or divergence of transformation flux. Referred to as the water-mass formation rate, it is estimated as $-\Delta\sigma(\partial A/\partial\sigma)$ (Marshall et al. 1999; Nishikawa et al. 2013). Analysis of the formation rate allows us to determine whether there is volume inflation or deflation within a specific density layer and further deduce the occurrence of balancing downwelling or upwelling.

The water-mass formation rate is given by the slope of the water-mass transformation curve in Fig. 5b. In winter, the highest transformation rate occurs around 26.1 kg m^{-3}, resulting in a negative water-mass formation rate for the density range smaller than this (Fig. 6b). This divergence implies upwelling in areas with surface density below 26.1 kg m^{-3}. However, for the density range larger than 26.1 kg m^{-3}, the water-mass formation rate is positive, and so convergence of transformation flux (Fig. 6b). Consequently, one can anticipate downwelling in regions with a surface density larger than 26.1 kg m^{-3}, as depicted in Fig. 6c. It should be noted that the convergence of the transformation flux is slightly larger than the divergence when considering the slope of the water-mass transformation rate (Fig. 5b).

The inferred wintertime water-mass formation is closely linked to the residual overturning circulation. The residual overturning streamfunction in winter perhaps does not accurately represent the flow, due to the nonzero tendency of

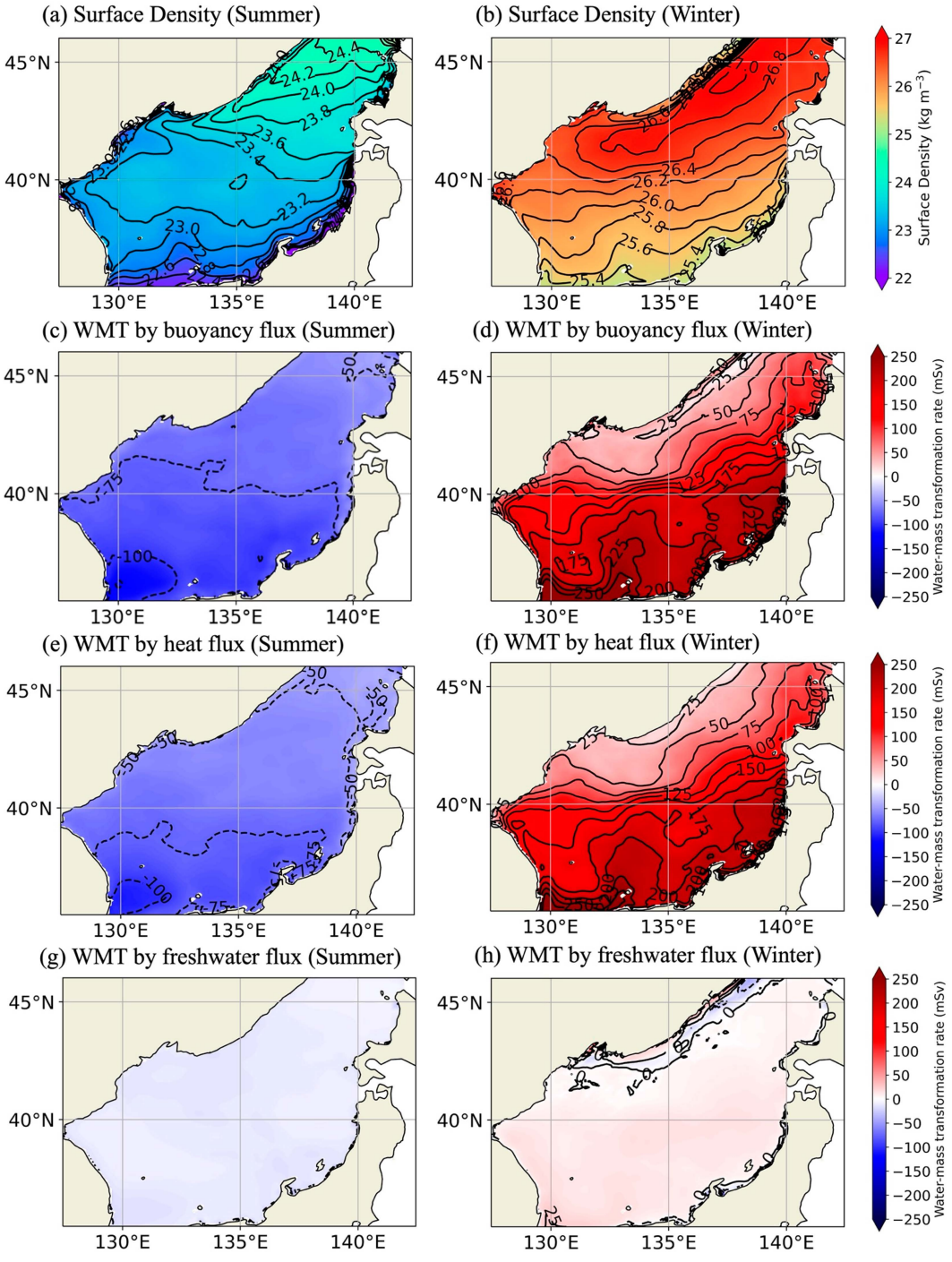

FIG. 4. (a),(b) Surface density (kg m^{-3}) and (c)–(h) water-mass transformation rate (m^3 s^{-1}) in (a),(c),(e),(g) summer (June–August) and (b),(d),(f),(h) winter (December–February), respectively, averaged over 1996–2015. The contributions to water-mass transformation are due to (c),(d) surface buoyancy flux, (e),(f) heat flux, and (g),(h) freshwater flux.

layer thickness, and so requires caution in interpretation. However, it still provides insight into the general circulation pattern. Notably, the upwelling and downwelling patterns expected from the winter water-mass transformation rate are captured in the residual circulation streamfunction, indicating a connection between buoyancy forcing and the overturning circulation in the EJS. In Fig. 2b, the 26.1 kg m^{-3} isopycnal, corresponding to the highest water-mass transformation rate, outcrops near 39.5°N. Interestingly, the maximum residual overturning streamfunction is also located close to this

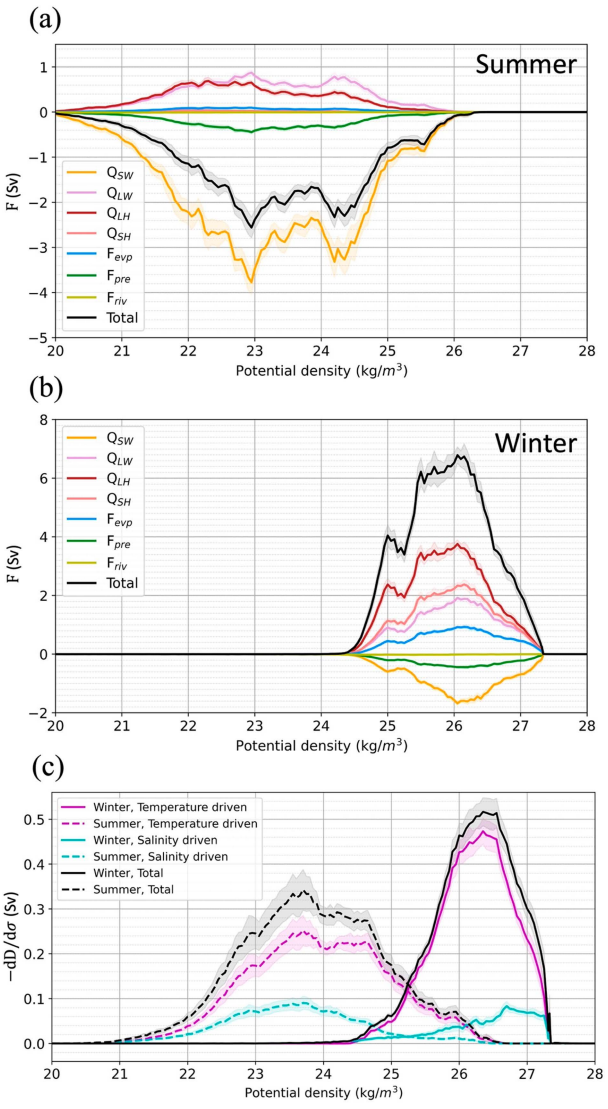

FIG. 5. Air–sea transformation rate ($\times 10^6$ m^3 s^{-1} or Sv) in (a) summer (June–August) and (b) winter (December–February). (c) Transformation rate due to diffusive fluxes at the base of the mixed layer. All values are averaged for 1996–2015. The Q_{SW}, Q_{LW}, Q_{LH}, and Q_{SH} are the transformation rates by shortwave radiation, longwave radiation, latent heat flux, and sensible heat flux, respectively, while F_{evp}, F_{pre}, and F_{riv} are the water-mass transformation rates by freshwater associated with evaporation, precipitation, and river runoff, respectively. Shading represents ±1 standard error.

latitude, and there is upwelling and downwelling to the south and north of that latitude, respectively (Fig. 6a), consistent with water-mass formation rates.

4. Discussion and conclusions

The East/Japan Sea (EJS), a marginal sea in the northwest Pacific, hosts a myriad of oceanic processes including a meridional overturning circulation. In this study, we investigate the residual circulation and water-mass transformation/formation rates in the EJS utilizing MITgcm, a general ocean circulation model capable of computing transport in density layers. The water-mass transformation and formation rates are obtained by accounting for both thermodynamic and kinematic processes in these density layers. The 20-yr simulation forced by ERA5 from 1996 to 2015 reveals residual circulation patterns in the EJS, showing considerable differences in pattern and intensity compared with the Eulerian circulation. The eddy-driven streamfunction is well developed near the sea surface acting to flatten isopycnals.

The water-mass transformation rates are also found to be substantially different between summer and winter. In summer, buoyancy gain by shortwave radiation dominates, resulting in a negative water-mass transformation rate in the EJS. Considering northward surface flow, this negative rate implies an isopycnal velocity which is faster than the flow itself, but in the opposite direction. In winter, contributions from turbulent (latent and sensible) heat flux and longwave radiation exceed that from shortwave radiation, leading to a positive water-mass transformation rate. The wintertime water-mass formation rate, derived from the first derivative of the transformation rate, is negative (positive) in the density range lower (higher) than 26.1 kg m^{-3}, indicating divergence (convergence). These results align with the pattern of residual overturning circulation which shows upwelling (downwelling) to the south (north) of approximately 39.5°N where the 26.1 kg m^{-3} isopycnal outcrops. Although the diapycnal volume flux due to diffusive fluxes is relatively small compared to that from surface density fluxes, it increases the density of the mixed layer throughout the year. This process is critical in shaping the residual circulation at the subsurface, which has density increasing along the subsurface flow.

The residual overturning streamfunction of the EJS has been presented here for the first time. Our study suggests that the eddy-driven streamfunction near the surface is significantly smaller than the Eulerian streamfunction in the region to the north of the Tsugaru Strait. However, it becomes comparable to the Eulerian streamfunction near the surface to the south of the Tsugaru Strait. The overturning circulation associated with transient eddies plays a significant role in the region south of the Tsugaru Strait, whereas that associated with standing eddies exerts a notable influence in the region north of the strait. This finding likely represents the eddy-driven streamfunction's contribution under conditions where the isopycnals are almost vertical in winter. This suggests that the Eulerian streamfunction might considerably overestimate the meridional overturning circulation and associated northward transport near the surface, underscoring the importance of eddy processes in the ocean circulation in winter and to the south of the Tsugaru Strait.

The observation of relatively high oxygen concentration near 1000 m indicates active ventilation in the EJS, unlike other North Pacific regions (Fig. 1a). This ventilation to depths below 1000 m is not captured by the derived residual overturning streamfunction (Figs. 3, 6), suggesting that deep/bottom water formation might be inadequately simulated. The absence of deep ventilation could be attributed to several factors: (i) model bias, particularly the failure to adequately

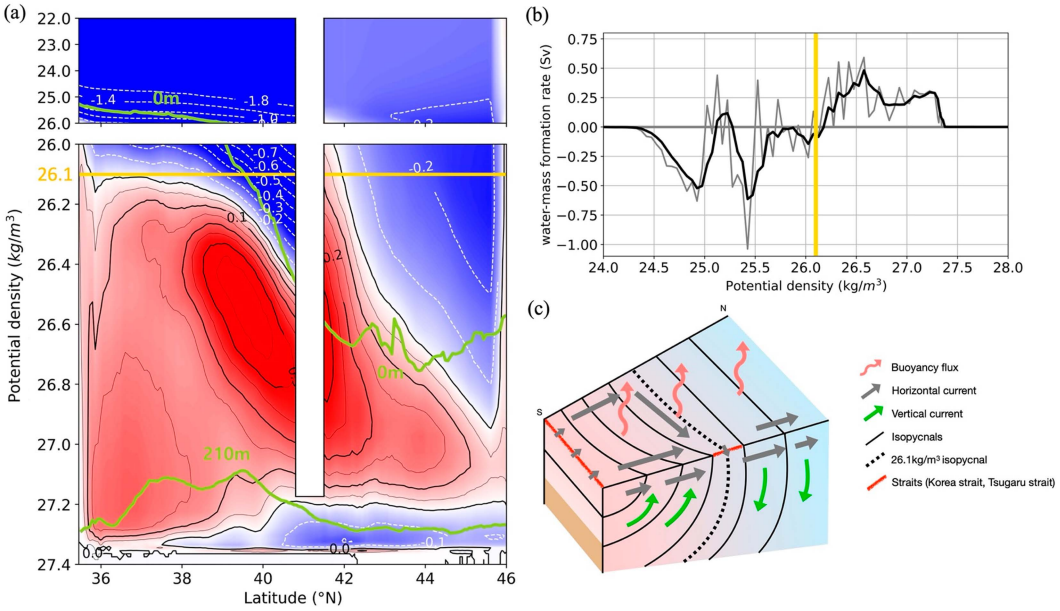

FIG. 6. (a) Winter (December–February) meridional residual overturning streamfunction (Sv) averaged over the period 1996–2015. Thick and thin black contours are at 0.1- and 0.05-Sv intervals, respectively. Light green lines represent the mean density at the surface and at 210 m. (b) Water-mass formation rate ($\times 10^6$ m^3 s^{-1} or Sv) given by the slope of Fig. 5b. The yellow line in (a) and (b) marks 26.1 kg m^{-3}, the density of the highest water-mass transformation rate in winter shown in Fig. 5b. (c) A schematic diagram showing the winter diapycnal volume flux [A in Eq. (8)] contributed by buoyancy flux [$\mathcal{B}_s$ in Eq. (12)] in the EJS. Because the diapycnal volume flux varies with latitude, there is upwelling (downwelling) in the south (north) of the 26.1 kg m^{-3} isopycnal.

simulate brine rejection; (ii) the relatively uniform abyssal potential density, which limits the expression of vertical motion in density space; (iii) the episodic nature of deep/bottom water formation through convection and brine rejection, which is too brief and localized to be captured in the temporally and zonally averaged residual overturning streamfunction; and (iv) the observed weakening of ventilation in the EJS since 1930 (Gamo et al. 1986; Gamo 1999; Kim et al. 1999; Talley et al. 2003). Although the deep/bottom water formation re-emerges in 2000–01 (Kim et al. 2002; Talley et al. 2006), warmer winters in a warming world lead to a decrease in deep convection in the EJS (Gamo 2011; Senjyu 2020; Senjyu and Shiota 2023).

The positive water-mass transformation in winter is mainly driven by turbulent heat fluxes, with latent and sensible heat fluxes being the main contributors in the EJS. This result can be compared to that found in the Gulf of Arabia, where latent heat flux is the dominant term followed by longwave radiation (Al-Shehhi et al. 2021). The ERA5 reanalysis suggests that sensible heat flux plays a larger role than longwave loss to the atmosphere in winter over the western boundary current regions (not shown). Situated near the western boundary current, the EJS is more strongly influenced by sensible than longwave flux in winter, consistent with our water-mass transformation analysis. The contribution from the sensible heat flux in summer is negligible, showing a large seasonality in the EJS.

This study provides an example of the orchestration between kinematic and thermodynamic processes. The divergence and convergence of the water-mass transformation rates suggest that upwelling and downwelling, respectively, are manifested in the residual circulation in winter. This tight connection between surface buoyancy fluxes and meridional overturning circulation suggests that one can anticipate changes in the meridional overturning circulation from the study of those buoyancy fluxes alone. Under a warming climate scenario, SST in the EJS is expected to increase faster than the global mean trend (Sung et al. 2021). One might then expect this warming to result in a slowing of the meridional overturning circulation and an increase in upper-ocean stratification. That said, the future state of the meridional overturning circulation is best inferred from changes in buoyancy fluxes and not just from expected changes in SST. In addition, the eddy-driven circulation, which is not easily obtained from global ocean models, plays a critical role in the meridional overturning circulation. In this context, dynamical downscaling of global climate models could be performed to yield a more accurate projection of the meridional overturning circulation in the EJS.

Acknowledgments. This work was supported by the National Research Foundation of Korea (NRF) grant funded by the Korean government (MSIT) (2018R1A5A1024958, NRF-2022R1A2C1009792) and the Korea Meteorological Administration Research and Development Program under Grant (RS-2024-00404973). J. M. would like to thank the Physical Oceanography program of NASA for their support.

Data availability statement. The MITgcm configuration used for this study is available at the website (https://github.com/yujink7/MITgcm-configuration.git), and the LLC_1080 configuration can be obtained from https://github.com/MITgcm-contrib/llc_hires/tree/master/llc_1080. The GEBCO bathymetry data are available at GEBCO (https://www.gebco.net). The model boundary, initial conditions, and atmospheric forcing are available at ORAS5 (https://cds.climate.copernicus.eu), ERA5 (https://www.ecmwf.int), and JRA55-do (https://aims2.llnl.gov/search/input4mips). The tidal forcing is derived from OTPS (https://www.tpxo.net/otps). The climate volume fraction of oxygen and sea surface salinity are from *WOA2013* (https://www.ncei.noaa.gov/products/world-ocean-atlas). The sea level anomaly data are available at CMEMS (https://data.marine.copernicus.eu/products). The temperature data for comparing model result with observation were obtained from the National Centers for Environmental Information (https://www.ncei.noaa.gov/products) and the National Institute of Fisheries Science (NIFS) (https://www.nifs.go.kr). Eddy kinetic energy observation data are from AVISO (www.aviso.altimetry.fr).

APPENDIX

Model Simulations

We performed a series of simulations over the northwest Pacific using MITgcm using various configurations and datasets as listed in Table A1. The resulting ocean circulation patterns share similar large-scale features. For example, although differing in strength and extent, the residual circulation from seven different model simulations is comparable with each other (Fig. A1). This suggests that the presented meridional overturning structure in the EJS is consistent.

TABLE A1. Model simulations which have little difference in the result.

	Initial condition	Boundary condition	Atmospheric forcing	River runoff	SSS nudging period	Sea ice package
Paper	*WOA2013* (*T*, *S*), ORAS5	ORAS5	ERA5	JRA-55	1 month	O
1	ORAS5	ORAS5	ERA5	JRA-55	1 month	O
2	ORAS5	ORAS5	ERA5	JRA-55 (partially masked)	1 month	O
3	ORAS5	ORAS5	ERA5	JRA-55	6 months	O
4	ORAS5	ORAS5	ERA-Interim	JRA-55 (diffused river)	—	O
5	ORAS5	ORAS5	ERA5	JRA-55	1 month	X
6	HYCOM (*T*, *S*), ORAS5	ORAS5	ERA5	JRA-55	1 month	O
7	HYCOM, ORAS5 (Sea Ice)	HYCOM, ORAS5 (Sea Ice)	ERA5	JRA-55	1 month	O

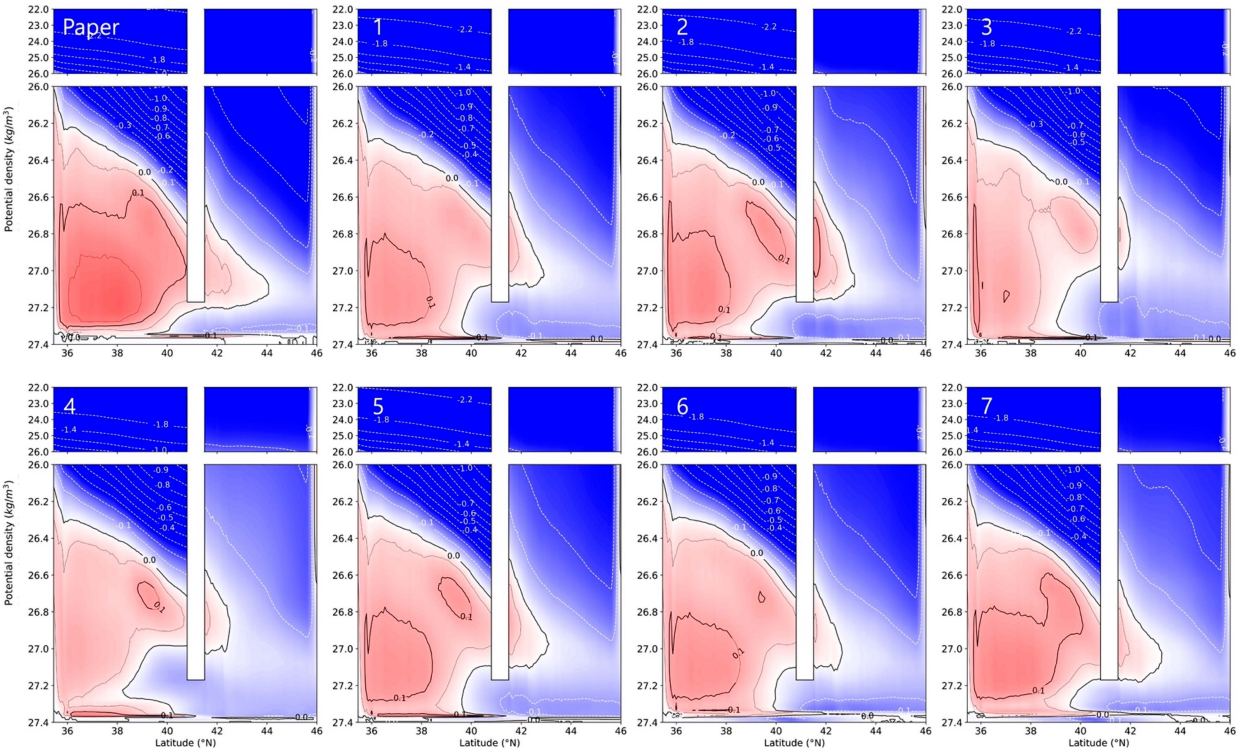

FIG. A1. Residual overturning streamfunction (Sv) averaged for 1996–2015 for model simulations in Table A1.

REFERENCES

Abernathey, R., J. Marshall, and D. Ferreira, 2011: The dependence of Southern Ocean meridional overturning on wind stress. *J. Phys. Oceanogr.*, **41**, 2261–2278, https://doi.org/10.1175/JPO-D-11-023.1.

Abernathey, R. P., I. Cerovecki, P. R. Holland, E. Newsom, M. Mazloff, and L. D. Talley, 2016: Water-mass transformation by sea ice in the upper branch of the Southern Ocean overturning. *Nat. Geosci.*, **9**, 596–601, https://doi.org/10.1038/ngeo2749.

Al-Shehhi, M. R., H. Song, J. Scott, and J. Marshall, 2021: Water mass transformation and overturning circulation in the Arabian Gulf. *J. Phys. Oceanogr.*, **51**, 3513–3527, https://doi.org/10.1175/JPO-D-20-0249.1.

Andrews, D. G., J. R. Holton, and C. B. Leovy, 1987: *Middle Atmosphere Dynamics*. International Geophysics Series, Vol. 40, Academic Press, 489 pp.

Arakawa, A., and V. R. Lamb, 1977: Computational design of the basic dynamical processes of the UCLA general circulation model. *Methods in Computational Physics*, J. Chang, Ed., Vol. 17, Academic Press, 173–265.

Buckley, M. W., and J. Marshall, 2016: Observations, inferences, and mechanisms of the Atlantic meridional overturning circulation: A review. *Rev. Geophys.*, **54**, 5–63, https://doi.org/10.1002/2015RG000493.

Cessi, P., 2019: The global overturning circulation. *Annu. Rev. Mar. Sci.*, **11**, 249–270, https://doi.org/10.1146/annurev-marine-010318-095241.

Choi, Y. J., and J.-H. Yoon, 2010: Structure and seasonal variability of the deep mean circulation of the East Sea (Sea of Japan). *J. Oceanogr.*, **66**, 349–361, https://doi.org/10.1007/s10872-010-0031-y.

Choi, J., K. E. Lee, and H. J. Lee, 2012: Spatial and temporal changes in sea surface temperature, circulation and subpolar front of the East Sea (Japan Sea) during the last 130,000 years. *Palaeogeogr. Palaeoclimatol. Palaeoecol.*, **313–314**, 225–233, https://doi.org/10.1016/j.palaeo.2011.11.002.

Choi, B.-J., S. H. Cho, H. S. Jung, S.-H. Lee, D.-S. Byun, and K. Kwon, 2018: Interannual variation of surface circulation in the Japan/East Sea due to external forcings and intrinsic variability. *Ocean Sci. J.*, **53**, 1–16, https://doi.org/10.1007/s12601-017-0058-8.

Danchenkov, M. A., and S. C. Riser, 2000: Observations of currents, temperature and salinity in the Japan Sea in 1999–2000 by palace floats. *Dimensions*, **900**, 17.

Dufour, C. O., J. Le Sommer, J. D. Zika, M. Gehlen, J. C. Orr, P. Mathiot, and B. Barnier, 2012: Standing and transient eddies in the response of the Southern Ocean meridional overturning to the southern annular mode. *J. Climate*, **25**, 6958–6974, https://doi.org/10.1175/JCLI-D-11-00309.1.

Egbert, G. D., and S. Y. Erofeeva, 2002: Efficient inverse modeling of barotropic ocean tides. *J. Atmos. Oceanic Technol.*, **19**, 183–204, https://doi.org/10.1175/1520-0426(2002)019<0183:EIMOBO>2.0.CO;2.

Feng, Y., D. Menemenlis, H. Xue, H. Zhang, D. Carroll, Y. Du, and H. Wu, 2021: Improved representation of river runoff in Estimating the Circulation and Climate of the Ocean Version 4 (ECCOv4) simulations: Implementation, evaluation, and impacts to coastal plume regions. *Geosci. Model Dev.*, **14**, 1801–1819, https://doi.org/10.5194/gmd-14-1801-2021.

Gamo, T., 1999: Global warming may have slowed down the deep conveyor belt of a marginal sea of the northwestern Pacific: Japan Sea. *Geophys. Res. Lett.*, **26**, 3137–3140, https://doi.org/10.1029/1999GL002341.

——, 2011: Dissolved oxygen in the bottom water of the Sea of Japan as a sensitive alarm for global climate change. *Trends Anal. Chem.*, **30**, 1308–1319, https://doi.org/10.1016/j.trac.2011.06.005.

——, Y. Nozaki, H. Sakai, T. Nakai, and H. Tsubota, 1986: Spacial and temporal variations of water characteristics in the Japan Sea bottom layer. *J. Mar. Res.*, **44**, 781–793.

Groeskamp, S., S. M. Griffies, D. Iudicone, R. Marsh, A. J. Nurser, and J. D. Zika, 2019: The water mass transformation framework for ocean physics and biogeochemistry. *Annu. Rev. Mar. Sci.*, **11**, 271–305, https://doi.org/10.1146/annurev-marine-010318-095421.

Han, M., Y.-K. Cho, H.-W. Kang, and S. Nam, 2020: Decadal changes in meridional overturning circulation in the East Sea (Sea of Japan). *J. Phys. Oceanogr.*, **50**, 1773–1791, https://doi.org/10.1175/JPO-D-19-0248.1.

——, Y. S. Chang, H.-W. Kang, D.-J. Kang, and Y. S. Kim, 2021: Turnover time of the East Sea (Sea of Japan) meridional overturning circulation. *Front. Mar. Sci.*, **8**, 768899, https://doi.org/10.3389/fmars.2021.768899.

Hersbach, H., and Coauthors, 2020: The ERA5 global reanalysis. *Quart. J. Roy. Meteor. Soc.*, **146**, 1999–2049, https://doi.org/10.1002/qj.3803.

——, and Coauthors, 2023: ERA5 hourly data on pressure levels from 1940 to present. Copernicus Climate Change Service (C3S) Climate Data Store (CDS), accessed 17 May 2021, https://doi.org/10.24381/cds.bd0915c6.

Ichiye, T., 1984: Some problems of circulation and hydrography of the Japan Sea and the Tsushima Current. *Elsevier Oceanogr. Ser.*, **39**, 15–54, https://doi.org/10.1016/S0422-9894(08)70289-7.

Isobe, A., 2008: Recent advances in ocean-circulation research on the Yellow Sea and East China Sea shelves. *J. Oceanogr.*, **64**, 569–584, https://doi.org/10.1007/s10872-008-0048-7.

Jayasankar, T., R. Murtugudde, and T. I. Eldho, 2019: The Indian Ocean deep meridional overturning circulation in three ocean reanalysis products. *Geophys. Res. Lett.*, **46**, 12 146–12 155, https://doi.org/10.1029/2019GL084244.

Kang, H., and C. N. K. Mooers, 2005: Diagnoses of simulated water-mass subduction/formation/transformation in the Japan/East Sea (JES). *Deep-Sea Res. II*, **52**, 1505–1524, https://doi.org/10.1016/j.dsr2.2004.06.039.

Kawamura, H., J.-H. Yoon, and T. Ito, 2007: Formation rate of water masses in the Japan Sea. *J. Oceanogr.*, **63**, 243–253, https://doi.org/10.1007/s10872-007-0025-6.

Kim, K., K.-R. Kim, D.-H. Min, Y. Volkov, J.-H. Yoon, and M. Takematsu, 2001: Warming and structural changes in the East (Japan) Sea: A clue to future changes in global oceans? *Geophys. Res. Lett.*, **28**, 3293–3296, https://doi.org/10.1029/2001GL013078.

Kim, K.-R., K. Kim, D.-J. Kang, S. Y. Park, M.-K. Park, Y.-G. Kim, H. S. Min, and D. Min, 1999: The East Sea (Japan Sea) in change: A story of dissolved oxygen. *Mar. Technol. Soc. J.*, **33**, 15–22, https://doi.org/10.4031/MTSJ.33.1.3.

——, G. Kim, K. Kim, V. Lobanov, V. Ponomarev, and A. Salyuk, 2002: A sudden bottom-water formation during the severe winter 2000–2001: The case of the East/Japan Sea. *Geophys. Res. Lett.*, **29**, 1234, https://doi.org/10.1029/2001GL014498.

Koch-Larrouy, A., G. Madec, D. Iudicone, A. Atmadipoera, and R. Molcard, 2008: Physical processes contributing to the water mass transformation of the Indonesian throughflow. *Ocean Dyn.*, **58**, 275–288, https://doi.org/10.1007/s10236-008-0154-5.

Large, W. G., and S. Pond, 1981: Open ocean momentum flux measurements in moderate to strong winds. *J. Phys. Oceanogr.*, **11**, 324–336, https://doi.org/10.1175/1520-0485(1981)011<0324:OOMFMI>2.0.CO;2.

——, and ——, 1982: Sensible and latent heat flux measurements over the ocean. *J. Phys. Oceanogr.*, **12**, 464–482, https://doi.org/10.1175/1520-0485(1982)012<0464:SALHFM>2.0.CO;2.

——, J. C. McWilliams, and S. C. Doney, 1994: Oceanic vertical mixing: A review and a model with nonlocal boundary layer parameterization. *Rev. Geophys.*, **32**, 363–403, https://doi.org/10.1029/94RG01872.

Levitus, S., and Coauthors, 2015: World Ocean Atlas 2013 (NCEI Accession 0114815). NOAA National Centers for Environmental Information, accessed 7 September 2022, https://doi.org/10.7289/v5f769gt.

Locarnini, R. A., and Coauthors, 2013: *Temperature*. Vol. 1, *World Ocean Atlas 2013*, NOAA Atlas NESDIS 73, 40 pp., https://data.nodc.noaa.gov/woa/WOA13/DOC/woa13_vol1.pdf.

Losch, M., D. Menemenlis, J.-M. Campin, P. Heimbach, and C. Hill, 2010: On the formulation of sea-ice models. Part 1: Effects of different solver implementations and parameterizations. *Ocean Modell.*, **33**, 129–144, https://doi.org/10.1016/j.ocemod.2009.12.008.

Marshall, J., and T. Radko, 2003: Residual-mean solutions for the Antarctic Circumpolar Current and its associated overturning circulation. *J. Phys. Oceanogr.*, **33**, 2341–2354, https://doi.org/10.1175/1520-0485(2003)033<2341:RSFTAC>2.0.CO;2.

——, and K. Speer, 2012: Closure of the meridional overturning circulation through Southern Ocean upwelling. *Nat. Geosci.*, **5**, 171–180, https://doi.org/10.1038/ngeo1391.

——, A. Adcroft, C. Hill, L. Perelman, and C. Heisey, 1997a: A finite-volume, incompressible Navier Stokes model for studies of the ocean on parallel computers. *J. Geophys. Res. Oceans*, **102**, 5753–5766, https://doi.org/10.1029/96JC02775.

——, C. Hill, L. Perelman, and A. Adcroft, 1997b: Hydrostatic, quasi-hydrostatic, and nonhydrostatic ocean modeling. *J. Geophys. Res. Oceans*, **102**, 5733–5752, https://doi.org/10.1029/96JC02776.

——, D. Jamous, and J. Nilsson, 1999: Reconciling thermodynamic and dynamic methods of computation of water-mass transformation rates. *Deep-Sea Res. I*, **46**, 545–572, https://doi.org/10.1016/S0967-0637(98)00082-X.

Min, D.-H., and M. J. Warner, 2005: Basin-wide circulation and ventilation study in the East Sea (Sea of Japan) using chlorofluorocarbon tracers. *Deep-Sea Res. II*, **52**, 1580–1616, https://doi.org/10.1016/j.dsr2.2003.11.003.

Mooers, C. N. K., H. Kang, I. Bang, and D. P. Snowden, 2006: Some lessons learned from comparisons of numerical simulations and observations of the JES circulation. *Oceanography*, **19**, 86–95, https://doi.org/10.5670/oceanog.2006.46.

Nishikawa, S., H. Tsujino, K. Sakamoto, and H. Nakano, 2013: Diagnosis of water mass transformation and formation rates in a high-resolution GCM of the North Pacific. *J. Geophys. Res. Oceans*, **118**, 1051–1069, https://doi.org/10.1029/2012JC008116.

Park, J. J., and K. Kim, 2013: Deep currents obtained from Argo float trajectories in the Japan/East Sea. *Deep-Sea Res. II*, **85**, 169–181, https://doi.org/10.1016/j.dsr2.2012.07.032.

Park, Y.-G., J.-H. Park, H. J. Lee, H. S. Min, and S.-D. Kim, 2013: The effects of geothermal heating on the East/Japan Sea circulation. *J. Geophys. Res. Oceans*, **118**, 1893–1905, https://doi.org/10.1002/jgrc.20161.

Pinardi, N., P. Cessi, F. Borile, and C. L. P. Wolfe, 2019: The Mediterranean Sea overturning circulation. *J. Phys. Oceanogr.*, **49**, 1699–1721, https://doi.org/10.1175/JPO-D-18-0254.1.

Plumb, R. A., and J. D. Mahlman, 1987: The zonally averaged transport characteristics of the GFDL general circulation/transport model. *J. Atmos. Sci.*, **44**, 298–327, https://doi.org/10.1175/1520-0469(1987)044<0298:TZATCO>2.0.CO;2.

Riser, S. C., and G. Jacobs, 2005: The Japan/East Sea: A historical and scientific introduction. *Deep-Sea Res. II*, **52**, 1359–1362, https://doi.org/10.1016/j.dsr2.2005.05.002.

Senjyu, T., 2020: Long-term changes in the abyssal Japan Sea (East Sea): A physical view. *Changing Asia-Pacific Marginal Seas*, C.-T. A. Chen and X. Guo, Eds., Atmosphere, Earth, Ocean & Space, Springer, 69–85, https://doi.org/10.1007/978-981-15-4886-4_5.

——, and K. Shiota, 2023: Revisit the upper portion of the Japan sea proper water: A recent structural change and freshening in the formation area. *J. Geophys. Res. Oceans*, **128**, e2022JC019094, https://doi.org/10.1029/2022JC019094.

——, H.-R. Shin, J.-H. Yoon, Z. Nagano, H.-S. An, S.-K. Byun, and C.-K. Lee, 2005: Deep flow field in the Japan/East Sea as deduced from direct current measurements. *Deep-Sea Res. II*, **52**, 1726–1741, https://doi.org/10.1016/j.dsr2.2003.10.013.

Stewart, A. L., 2021: Mesoscale, tidal, and seasonal/interannual drivers of the Weddell Sea overturning circulation. *J. Phys. Oceanogr.*, **51**, 3695–3722, https://doi.org/10.1175/JPO-D-20-0320.1.

Sung, H. M., J. Kim, J.-H. Lee, S. Shim, K.-O. Boo, J.-C. Ha, and Y.-H. Kim, 2021: Future changes in the global and regional sea level rise and sea surface temperature based on CMIP6 models. *Atmosphere*, **12**, 90, https://doi.org/10.3390/atmos12010090.

Talley, L. D., V. Lobanov, V. Ponomarev, A. Salyuk, P. Tishchenko, I. Zhabin, and S. Riser, 2003: Deep convection and brine rejection in the Japan Sea. *Geophys. Res. Lett.*, **30**, 1159, https://doi.org/10.1029/2002GL016451.

——, and Coauthors, 2006: Japan/East Sea water masses and their relation to the sea's circulation. *Oceanography*, **19** (3), 32–49, https://doi.org/10.5670/oceanog.2006.42.

Tsujino, H., and Coauthors, 2018: JRA-55 based surface dataset for driving ocean–sea-ice models (JRA55-do). *Ocean Modell.*, **130**, 79–139, https://doi.org/10.1016/j.ocemod.2018.07.002.

Walin, G., 1982: On the relation between sea-surface heat flow and thermal circulation in the ocean. *Tellus*, **34A**, 187–195, https://doi.org/10.3402/tellusa.v34i2.10801.

Wang, D., J. Xiao, Y. Shu, Q. Xie, J. Chen, and Q. Wang, 2016: Progress on deep circulation and meridional overturning circulation in the South China Sea. *Sci. China Earth Sci.*, **59**, 1827–1833, https://doi.org/10.1007/s11430-016-5324-6.

Weatherall, P., and Coauthors, 2015: A new digital bathymetric model of the world's oceans. *Earth Space Sci.*, **2**, 331–345, https://doi.org/10.1002/2015EA000107.

Wilson, E. A., A. F. Thompson, A. L. Stewart, and S. Sun, 2022: Bathymetric control of subpolar gyres and the overturning circulation in the Southern Ocean. *J. Phys. Oceanogr.*, **52**, 205–223, https://doi.org/10.1175/JPO-D-21-0136.1.

Xu, X., P. B. Rhines, and E. P. Chassignet, 2018: On mapping the diapycnal water mass transformation of the upper North Atlantic Ocean. *J. Phys. Oceanogr.*, **48**, 2233–2258, https://doi.org/10.1175/JPO-D-17-0223.1.

Yao, F., I. Hoteit, L. J. Pratt, A. S. Bower, P. Zhai, A. Köhl, and G. Gopalakrishnan, 2014: Seasonal overturning circulation in the Red Sea: 1. Model validation and summer circulation. *J. Geophys. Res. Oceans*, **119**, 2238–2262, https://doi.org/10.1002/2013JC009004.

Yoon, S.-T., and Coauthors, 2018: Re-initiation of bottom water formation in the East Sea (Japan Sea) in a warming world. *Sci. Rep.*, **8**, 1576, https://doi.org/10.1038/s41598-018-19952-4.

Yoshikawa, Y., C. M. Lee, and L. N. Thomas, 2012: The subpolar front of the Japan/East Sea. Part III: Competing roles of frontal dynamics and atmospheric forcing in driving ageostrophic vertical circulation and subduction. *J. Phys. Oceanogr.*, **42**, 991–1011, https://doi.org/10.1175/JPO-D-11-0154.1.

Zika, J. D., B. M. Sloyan, and T. J. McDougall, 2009: Diagnosing the Southern Ocean overturning from tracer fields. *J. Phys. Oceanogr.*, **39**, 2926–2940, https://doi.org/10.1175/2009JPO4052.1.

——, M. H. England, and W. P. Sijp, 2012: The ocean circulation in thermohaline coordinates. *J. Phys. Oceanogr.*, **42**, 708–724, https://doi.org/10.1175/JPO-D-11-0139.1.

Zuo, H., M. A. Balmaseda, S. Tietsche, K. Mogensen, and M. Mayer, 2019: The ECMWF operational ensemble reanalysis–analysis system for ocean and sea ice: A description of the system and assessment. *Ocean Sci.*, **15**, 779–808, https://doi.org/10.5194/os-15-779-2019.

Zweng, M., and Coauthors, 2013: *Salinity*. Vol. 2, *World Ocean Atlas 2013*, NOAA Atlas NESDIS 74, 39 pp., https://data.nodc.noaa.gov/woa/WOA13/DOC/woa13_vol2.pdf.